

# The equilibrium morphology of WC particles – A combined *ab initio* and experimental study

Yang Zhong, Hong Zhu, Leon L. Shaw\*, R. Ramprasad

Department of Chemical, Materials and Biomolecular Engineering, University of Connecticut, Storrs, CT 06269, USA

Received 25 November 2010; received in revised form 21 February 2011; accepted 8 March 2011

Available online 29 March 2011

## Abstract

We report an *ab initio* density functional theory study, complemented by parallel experimental work, of the equilibrium shape of WC particles. The equilibrium shape is simulated under the condition of little or no liquid-phase sintering. The effects of the carbon-rich and carbon-deficient conditions and the adsorption of Co and Ni atoms on the surface of WC particles are investigated. The equilibrium shape of WC particles is found to be a truncated triangular prism under both carbon-rich and carbon-deficient conditions. The adsorption of Co and Ni on the WC surface can promote the formation of either truncated triangular prisms or near-hexagonal prisms, depending on their specific combination with the carbon chemical potential. Under all the conditions investigated, the equilibrium shapes of WC crystals can be described as “bulky” rather than “plate-like”. The findings in this study are consistent with the experimental observations. © 2011 Acta Materialia Inc. Published by Elsevier Ltd. All rights reserved.

**Keywords:** Tungsten carbide; Crystal shape; *Ab initio* calculation; Cermets

## 1. Introduction

Cemented tungsten carbide with cobalt binder (WC/Co) has been widely used in military, aerospace, automotive, marine, petrochemical, mining, electronics and wood industries [1–4]. It is generally known that the hardness of WC/Co increases with decreasing crystal size of WC to the submicron or nanometer scale [5–12]. Many studies [10,11] also reveal that the fracture toughness decreases as the hardness increases. Thus, the size of WC crystals has a strong effect on the mechanical properties of WC/Co. In addition, some studies [13,14] have shown that the shape of WC crystals affects their mechanical properties. In particular, the formation of plate-like WC crystals has been reported to increase the fracture toughness of WC/Co [13,14]. Hence, a better understanding of the growth mechanism and equilibrium shape of WC is of great interest.

Towards this understanding, the size evolution of WC grains with time and temperature has been modeled using

Oswald ripening [15]. Both rounded and faceted WC grain growth [16], the grain growth at the free surface [17] and the formation mechanism of large WC crystals as well as twin structures [18] have been reported. Some work has also been devoted to study the early stage sintering, including the growth mechanisms [19] and the influence of the Co binder [19,20]. The effect of the carbon concentration on the microstructure evolution has been investigated [21], as has the effect of the metal additives [22,23]. WC crystals with the morphologies of triangular prisms [12,21,24] and truncated triangular prisms [12,13,21] have all been reported. These experimental studies have offered indispensable insights into the growth kinetics, growth mechanisms and shape of WC crystals during heating and sintering processes.

It is generally known that the growth of a crystal is governed by factors related to both thermodynamics (e.g. surface energies) and kinetics (e.g. activation energies for diffusion or adsorption/desorption). Thus, the shape of a crystal during growth may or may not be the equilibrium shape of that crystal, depending on whether the crystal growth is controlled by thermodynamics or kinetics. Sha-

\* Corresponding author. Tel.: +1 860 486 2592; fax: +1 860 486 4745.  
E-mail address: [leon.shaw@uconn.edu](mailto:leon.shaw@uconn.edu) (L.L. Shaw).

to et al. [25] pointed out that the shape of WC crystals in cemented carbide is determined by a balance of shape relaxation (towards the equilibrium structure) and carbide crystal growth processes (towards the growth-determined structure). They experimentally formed WC platelets in the cemented carbides [25,26], and studied the driving force for the shape relaxation and crystal growth using phenomenological thermodynamics [25]. Another promising approach to predict the equilibrium shape of grains and particles is the *ab initio* calculation in conjunction with the Wulff construction [27]. In this context, Christensen et al. [28–30] used the *ab initio* method to study the morphology of WC grains during liquid-phase sintering by calculating the interface energies between the WC particle and liquid Co. In their studies [29,30], an average value of the interfacial energies for several atomic configurations at the WC/Co interface or a value between the aforementioned average interfacial energy (which corresponds to an incoherent interface) and the minimum energy for a coherent interface was taken as the interfacial energy between WC and liquid Co. The effect of the carbon concentration on the morphology of WC grains is examined at two limiting chemical potentials for carbon, one being graphite (for the carbon-rich cermets) and the other the  $\eta$  phase (i.e.  $\text{Co}_3\text{W}_3\text{C}$  for the carbon-deficient cermets) [29,30]. Although some interesting results have been obtained, two critical issues remain unsolved: (i) the effects of different binder phases on the equilibrium morphology of WC crystals have not been explored; and (ii) the equilibrium morphology of WC crystals under the condition of little or no liquid phases is still an open issue.

Under the condition of little or no liquid phases, the equilibrium morphology of WC crystals is determined by the surface energy of WC particles rather than the interfacial energy between the WC and the liquid Co. Therefore, one may expect the equilibrium morphology of WC crystals under the condition of little or no liquid phases to be different from that under liquid-phase sintering. The necessity of investigating the equilibrium morphology of WC crystals under the condition of little or no liquid phases is further justified by the fact that solid-state sintering [31–36] and the formation of WC platelets in the solid state [18] have been reported by different groups. Therefore, the study of the equilibrium morphology of WC crystals in the solid state should provide a fundamental insight for better understanding the growth and sintering behavior of WC crystals during solid-state sintering.

In this study, we focus on addressing the two aforementioned issues, i.e. the binder effect and the equilibrium morphology of WC crystals during solid-state sintering, through a combination of the *ab initio* method and experimental investigation. For simulating WC grains during solid-state sintering of WC–Co cermets, we have studied the equilibrium morphology of WC particles with and without binder metal atoms adsorbed on the surface of WC crystals. Co and Ni, the two most common binders, are considered for this purpose. The morphology of WC

crystals predicted using this approach is then compared directly with specially designed experiments that do not entail liquid-phase sintering. This approach avoids the complication of liquid-phase sintering where the WC crystals are often in contact with other crystals and the shape can be truncated from the equilibrium form. The effect of the carbon concentration on the morphology of WC particles is examined at two limiting chemical potentials for carbon. One limit is graphite, which corresponds to the carbon-rich condition, and the other is  $\text{W}_2\text{C}$ , which corresponds to the carbon-deficient condition.  $\text{W}_2\text{C}$  is chosen because our previous study [37] reveals that the sequence of WC formation through the carburization of W and  $\text{Co}_3\text{W}$  is  $\text{W} + \text{Co}_3\text{W} \rightarrow \text{Co}_6\text{W}_6\text{C} \rightarrow \text{Co}_3\text{W}_3\text{C} \rightarrow \text{W}_2\text{C} \rightarrow \text{WC}$ . Thus, it is reasonable to assume that the first phase to form in the carbon-deficient condition is  $\text{W}_2\text{C}$ . The predicted shapes for Co-adsorbed WC crystals in carbon-rich and carbon-deficient conditions are found to be consistent with our experimental observations. The details of simulation, experiments and major findings are described below.

## 2. Computational model and methods

### 2.1. Methodology

The density functional theory (DFT) calculations are performed using the Vienna *ab initio* simulation package (VASP) [38,39], with the PW91 generalized gradient approximation (GGA) [40], the projector-augmented wave (PAW) treatment of electron–ion interactions and a cutoff energy of 400 eV for a plane wave expansion of the wave functions. The unit cell of bulk hexagonal WC is shown in Fig. 1a, which requires a Monkhorst–Pack  $k$ -point mesh of  $9 \times 9 \times 9$  for converged results. The calculated lattice parameters are 2.92 Å for  $a$  and 2.84 Å for  $c$ , in good agreement with the experimental values of the WC crystal [41].

It is established that the shape of hexagonal WC crystals in WC–Co cermets is bounded by prismatic  $\{10\bar{1}0\}$  surfaces and basal  $\{0001\}$  surfaces with two sets of three equivalent  $\{10\bar{1}0\}$  planes rather than six equivalent  $\{10\bar{1}0\}$  planes [13,24], as shown in Fig. 2. Thus, only these surfaces are investigated in the simulation. Two shape factors,  $r$  and  $k$ , are defined to describe the equilibrium shape. The parameter  $r$  is the ratio between the lengths of the short and long prismatic facets (cf. Fig. 2), while the aspect ratio  $k$  is defined as the ratio between the thickness along  $\langle 0001 \rangle$  direction ( $t$ ) and the width of the basal plane ( $w$ ),  $k = t/w$ .

Along the  $\langle 0001 \rangle$  and  $\langle 10\bar{1}0 \rangle$  directions of WC particles, the stacking sequence consists of alternating W and C planes (see Fig. 1a and b). As a result, WC is terminated either by W or C at the surfaces considered. W or C termination is enough to specify the  $\{0001\}$  surfaces because of the folding symmetry, as shown in Fig. 1a. For  $\{10\bar{1}0\}$  prismatic surfaces, however, there are two types of surfaces, denoted as type I and II surfaces, in addition to their W or C termination. In the type I surface, there are four

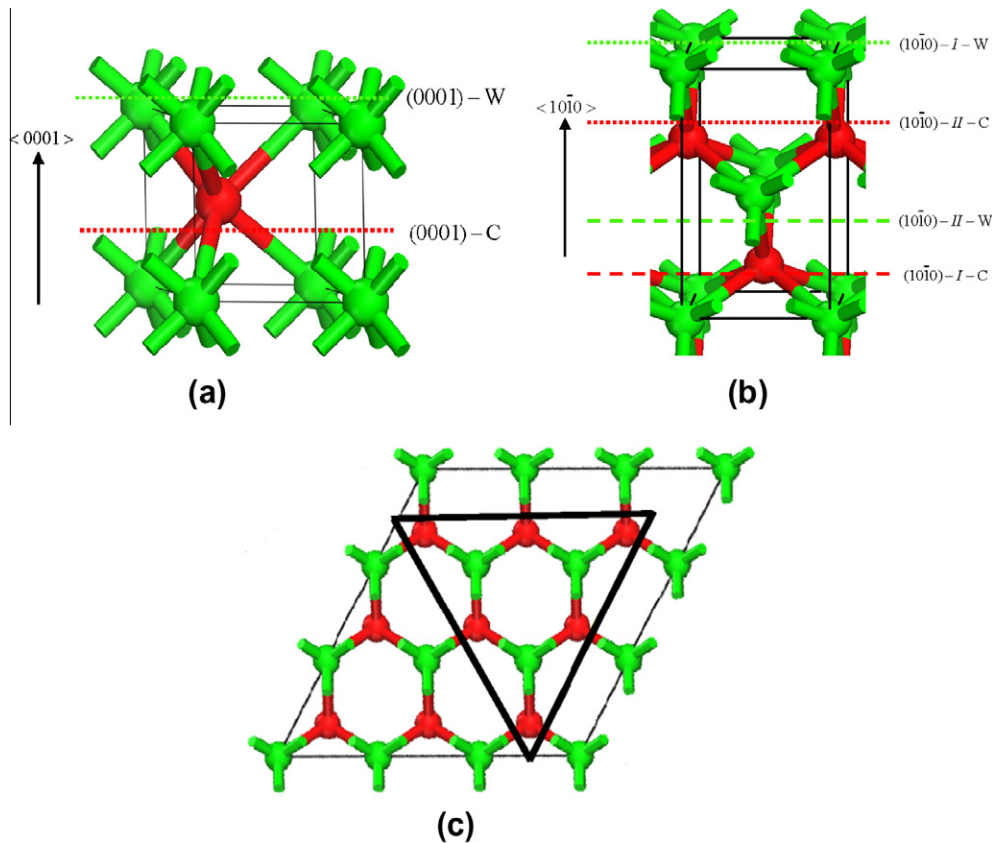


Fig. 1. (a) Side view of the WC unit cell, with the positions of the W and C terminations indicated; (b) side view of  $\{10\bar{1}0\}$  type surfaces, with the positions of all of the four possible terminations indicated; (c) top view of the  $(001)$  surface, with a triangle of the  $(10\bar{1}0)$ -II-C surfaces. Green and red spheres in (a–c) represent W and C atoms, respectively. (For interpretation of the references to color in this figure legend, the reader is referred to the web version of this article.)

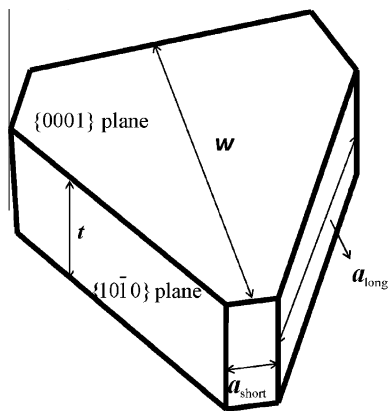


Fig. 2. Schematic of the equilibrium shape for a WC particle. The shape can be characterized by two shape factors, i.e.  $r = a_{\text{short}}/a_{\text{long}}$  and  $k = t/w$ .

dangling bonds per surface atom, while in the type II surface, there are only two dangling bonds, as shown in Fig. 1b. The energy differences among the basal plane, type I prismatic plane and type II prismatic plane will lead to the anisotropic morphology of WC particles. In order to study the equilibrium shape of WC particles, the following six kinds of surface facets have been considered in this study: (i) the W-terminated  $(0001)$  surface (denoted here-

inafter as 0001-W); (ii) the C-terminated  $(0001)$  surface ( $0001$ -C); (iii) the W-terminated type I  $(10\bar{1}0)$  surface ( $10\bar{1}0$ -I-W); (iv) the C-terminated type I  $(10\bar{1}0)$  surface ( $10\bar{1}0$ -I-C); (v) the W-terminated type II  $(10\bar{1}0)$  surface ( $10\bar{1}0$ -II-W); and (vi) the C-terminated type II  $(10\bar{1}0)$  surface ( $10\bar{1}0$ -II-C). The positions of these surface facets are indicated in Fig. 1a and b. By computing the surface energies, we can quantify the shape factors ( $r$  and  $k$ ) of WC particles and their dependence on the carbon potential before and after surface adsorption of Co and Ni atoms.

## 2.2. Thermodynamic details of the model

For  $(0001)$  surfaces (i.e. 0001-C and 0001-W), the standard symmetric supercell slab model is used to calculate the surface energies. The surface energy,  $\sigma_{\text{surf}}$ , is defined as [42]

$$\sigma_{\text{surf}} = (E_{\text{slab}} - E_{\text{bulk}})/2S \quad (1)$$

where  $E_{\text{slab}}$  and  $E_{\text{bulk}}$  are the energies of the slab and of the bulk material containing the same number and type of atoms.  $S$  is the surface area and the factor 2 accounts for the fact that we have two identical surfaces in the supercell.  $E_{\text{bulk}}$  could be expressed as

$$E_{\text{bulk}} = n_{\text{C}\mu\text{C}} + n_{\text{W}\mu\text{W}} \quad (2)$$

where  $\mu_C$  and  $\mu_W$  are the chemical potentials of C and W atoms in the bulk WC, and  $n_C$  and  $n_W$  are the number of C and W atoms in the surface slab, respectively. For one pair of W and C in the bulk WC, one can obtain its energy from Eq. (2) as  $E_{WC,bulk} = \mu_C + \mu_W$ , which is computed as a fixed value from the bulk hexagonal WC structure. Thus, the surface energy could be specified in term of  $\mu_C$  as follows:

$$\begin{aligned} \sigma_{surf} &= (E_{slab} - E_{bulk})/2S \\ &= [E_{slab} - n_W E_{WC,bulk} + (n_W - n_C)\mu_C]/2S \end{aligned} \quad (3)$$

By treating  $\mu_C$  as an independent parameter, we can determine the surface energy for both W- and C-terminated (0001) surfaces under both carbon-rich (larger  $\mu_C$ ) and carbon-deficient (smaller  $\mu_C$ ) conditions. In order to avoid the graphite segregation in the carbon-rich condition and the  $W_2C$  segregation in the carbon-deficient condition,  $\mu_C$  and  $\mu_W$  should comply with the following inequalities:

$$\mu_C < E_{graphite} \quad (4)$$

$$\mu_C + 2\mu_W < E_{W_2C} \quad (5)$$

where  $E_{graphite}$  stands for the chemical potential of a carbon atom in graphite and  $E_{W_2C}$  represents the chemical potential of two W and one C atoms in the lowest-energy form of  $W_2C$ , the  $\epsilon$ - $Fe_2N$  structure (space group  $P-31m$ ) [43]. Eqs. (4) and (5) correspond to the so-called “carbon-rich” and “carbon-deficient” conditions, respectively.

In the case of  $\{10\bar{1}0\}$  type surfaces, the surface energies cannot be solved with a standard slab supercell because of the lack of symmetry. As shown in Fig. 1b, there are four kinds of  $\{10\bar{1}0\}$  surfaces, namely  $10\bar{1}0$ -I-W,  $10\bar{1}0$ -I-C,  $10\bar{1}0$ -II-W and  $10\bar{1}0$ -II-C surfaces. To obtain the surface energies for all these four possible surfaces, we applied the wedge model with triangular cross-section [29,30] with all the three wedge facets to be  $10\bar{1}0$ -II-C sur-

faces, along with three normal slab supercells. As shown in Fig. 1c, the excess energy of the triangular wedge with respect to the bulk consists of the surface energy as well as the edge energy. The contribution from the latter to the excess energy decays with increasing side length of the triangle ( $L$ ). Fig. 3 plots the excess energy as a function of the reciprocal of the side length of the triangle for carbon-rich conditions ( $1/L$ ). With the length approaching infinity (i.e. the reciprocal close to 0), the excess energy of the triangle equals the surface energy, as indicated by the intercept of the curve with the  $y$ -axis ( $0.2119 \text{ eV } \text{\AA}^{-2}$ ). After solving the surface energies for  $10\bar{1}0$ -II-C, one can solve for the surface energies of the other three  $\{10\bar{1}0\}$  surfaces based on three normal supercell calculations, with the two surfaces being the  $(10\bar{1}0)$  type II facet and the  $(10\bar{1}0)$  type I facet, respectively.

Co and Ni, as the most common binder materials for WC, were selected as the adsorbed metals (M) to study the binder effect on the equilibrium shape of WC crystals.

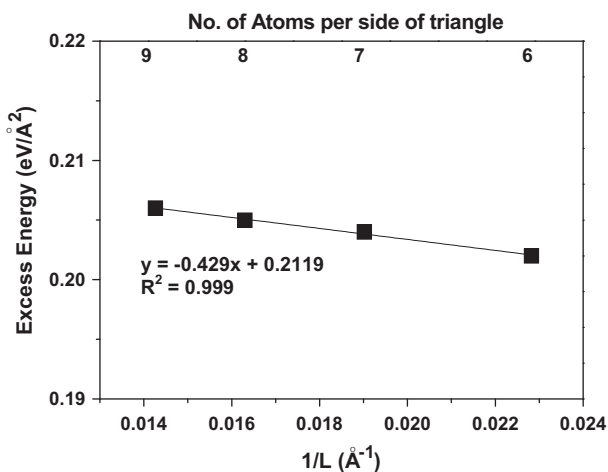


Fig. 3. The excess energy calculated in the carbon-rich condition as a function of the reciprocal of the side length ( $1/L$ ) of the triangle terminated by  $(10\bar{1}0)$ -II-C, which is shown in Fig. 1c. The surface energy for  $(10\bar{1}0)$ -II-C surfaces can be achieved by the extrapolation of the calculated energies to  $1/L = 0$ .

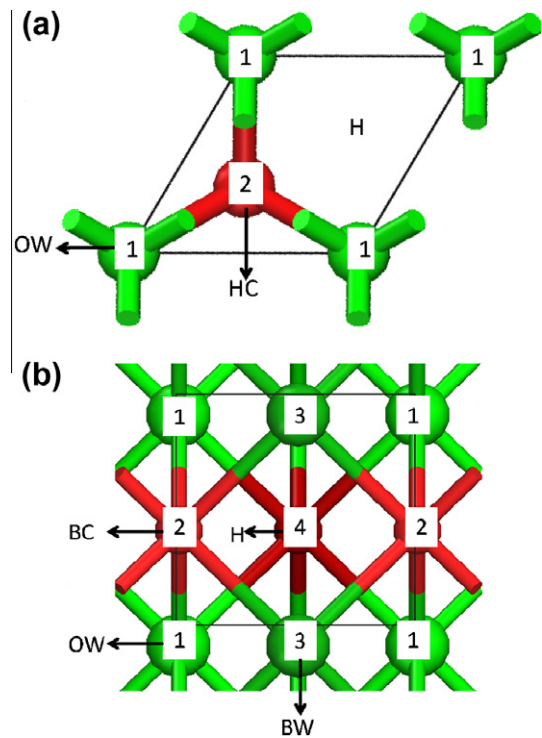


Fig. 4. (a) Top view of (0001) W-terminated surface. The possible sites where M may sit are on top of the surface W atom (OW), on top of the hollow where there is no C atom in the next layer (H) and on top of the hollow where C atom sits in the next layer (HC). (b) Top view of W-terminated  $\{10\bar{1}0\}$  surfaces. The possible sites where M may sit are on top of the surface W atom (OW), on top of the bridge between two neighboring W atoms with the C atom in the next layer (BC), on top of the bridge between two neighboring W atoms with the W atom in the third layer (BW) and on top of the hollow where C atom sits in the fourth layer (H). Green and red spheres represent W and C atoms, respectively. The number at each location represents the number of the layer with respect to the surface. Thus, 1 means the atom is on the surface, while 2, 3 and 4 mean the atoms are on the second, third and fourth  $\{10\bar{1}0\}$  layers from the surface, respectively. The situations are similar for the C-terminated surfaces.

For W-terminated  $\{0\ 0\ 0\ 1\}$  surfaces, M can be put on top of the surface W atom (OW), on top of the hollow where there is no C atom in the next layer (H) and on top of the hollow where the C atom sits in the next layer (HC), as shown in Fig. 4(a). For W-terminated  $\{1\ 0\ \bar{1}\ 0\}$  surfaces, M may be on top of the surface W atom (OW), on top of the bridge between two neighboring W atoms with the C atom in the next layer (BC), on top of the bridge between two neighboring W atoms with the W atom in the third layer (BW) and on top of the hollow where the C atom sits in the fourth layer (H), as shown in Fig. 4b. For C-terminated surfaces, the possible sites of the absorbed M are similar. The standard slab geometry can be used to create slabs with two different surfaces, i.e. one pure WC surface with the known surface energy of  $\sigma_{\text{surf}}$  and the other surface with adsorption of a M atom. By calculating the total surface energy of the two different surfaces, the surface energy for the facet with adsorption of an M atom can be derived from the difference between the total surface energy and the surface energy for the pure WC surface, expressed in Eq. (6):

$$\sigma_{\text{M-surf}} = (E'_{\text{slab}} - E_{\text{bulk}} - E_{\text{M}})/S - \sigma_{\text{surf}} \quad (6)$$

where  $E'_{\text{slab}}$  is the energy of the slab with one pure WC surface of known energy and one surface adsorbed with M atom,  $E_{\text{M}}$  is the energy of M in its elemental state, and  $\sigma_{\text{surf}}$  and  $E_{\text{bulk}}$  are as defined in Eq. (3).

### 3. Experimental

Some experiments were conducted for comparison with the simulation results. A commercial WC–5.8 wt.% Co powder of 99.9% purity with ~0.2% free carbon (Alfa Aesar, Ward Hill, MA) was used in the experiments. Because of the presence of ~0.2% free carbon, the as-received powder is in the carbon-rich condition. The carbon-deficient condition is created by heating the as-received powder in a tube furnace at 800 °C under an H<sub>2</sub> atmosphere for 2 h. This treatment has been proven to be an effective method to remove free carbon in carbide materials [44]. In order to confirm the creation of a carbon-deficient condition, the carbon contents in the WC–Co powders before and after the H<sub>2</sub> treatment were determined using an Elementar combustion analyzer (Elementar Analysensysteme, Germany). X-ray diffraction (XRD) was also performed with Cu K<sub>α</sub> radiation (Bruker Axs D5005D X-ray diffractometer) to identify the phases before and after the H<sub>2</sub> treatment. The particle sizes of the as-received WC–Co powder ranged from 100 to 700 nm, and no particle growth was found during the hydrogen treatment at 800 °C.

To study the morphology of WC particles, the carbon-rich and carbon-deficient powders were subjected to a heat treatment at 1400 °C for 2 h under an argon atmosphere in loose powder form. To ensure that the carbon-rich and carbon-deficient conditions are maintained during heat treatment, the carbon-deficient powder is loaded in an Al<sub>2</sub>O<sub>3</sub>

boat, whereas the carbon-rich powder is loaded into a graphite crucible within a glovebox filled with argon and sealed before heating. An Al<sub>2</sub>O<sub>3</sub> tube furnace evacuated to 10<sup>−3</sup> torr and then back filled with argon is used for both types of heat treatment. Sintering of the as-received WC–5.8 wt.% Co at the carbon-rich condition was also conducted at 1450 °C in argon for 24 h. The green WC–Co pellets for sintering are prepared by uniaxial pressing of 780 MPa in a steel die. The sintering temperature and time are higher and longer, respectively, than those of the heat treatment described above to ensure the sufficient growth of WC particles during sintering. It should be noted that the growth of WC particles becomes difficult during sintering, due to the physical contact of neighboring WC particles after powder compaction. The morphologies of the heat-treated powders and sintered WC–Co bodies are characterized with the aid of a field-emission scanning electron microscope (FESEM, JEOL, JSM 6335F).

## 4. Results and discussion

### 4.1. Effects of the carbon chemical potential

Table 1 lists the surface energies for all the facets considered in the carbon-rich and carbon-deficient conditions. The surface energies for  $\{1\ 0\ \bar{1}\ 0\}$  facets in the carbon-rich condition agree well with the prior work [30]. The deviation between our results and the prior work under carbon-deficient conditions is due to the different definitions of the carbon chemical potential (which is set by the W<sub>2</sub>C phase in the present study rather than the previously used η phase [30]). It can be seen from Table 1 that the W-terminated basal planes and prismatic planes are stable for the entire range of the allowed  $\mu_{\text{C}}$  due to their low surface energies compared with C-terminated facets. The only exception to this general rule is the type II prism plane in the carbon-rich condition. It can also be seen that type I prismatic facets have higher surface energies than type II prismatic facets and basal facets, which can be justified by the larger number of dangling bonds per surface atom in type I surfaces. This result suggests that the short prismatic facets of a WC particle with an equilibrium shape will be composed of type I surfaces, while the long prismatic facets will be composed of type II surfaces under both carbon-rich and carbon-deficient conditions. Overall, it can be expected that the energy differences among the basal plane, type I and type II prismatic planes will determine the equilibrium shape of the WC crystal and contribute to its anisotropic growth.

### 4.2. Effects of Co and Ni adsorption

The surface energies for the basal and prismatic planes were calculated with the adsorption of Co or Ni at various positions (cf. Fig. 4). Table 2 summarizes the results for the most favored (or lowest energy) adsorption site for each of the six classes of facets we considered. Note that adsorp-

Table 1  
Calculated surface energies for basal and prism planes in carbon-rich and carbon-deficient conditions.

Surface ID	Surface type	Termination	No. of dangling bonds	Surface energy (eV Å <sup>-2</sup> )*			
				W <sub>2</sub> C (C deficient)		Graphite (C rich)	
				This work	Ref. [16]	This work	Ref. [16]
0001-W	(0001)	W	3	<u>0.1869</u>		<u>0.2243</u>	
0001-C	(0001)	C	3	0.3994		0.3619	
10 $\bar{1}$ 0-I-W	(10 $\bar{1}$ 0) I	W	4	<u>0.2791</u>	0.3177	<u>0.3236</u>	0.3364
10 $\bar{1}$ 0-I-C	(10 $\bar{1}$ 0) I	C	4	0.5893	0.5468	0.5448	0.5287
10 $\bar{1}$ 0-II-W	(10 $\bar{1}$ 0) II	W	2	<u>0.2183</u>	0.2334	0.2405	0.2422
10 $\bar{1}$ 0-II-C	(10 $\bar{1}$ 0) II	C	2	0.2341	0.2191	<u>0.2119</u>	0.2103

\* The underlined numbers are the lowest energy for each type of the surface.

tion of Co and Ni (especially Ni) on type I facets can reduce surface energies substantially in comparison with clean facets, whereas the decrease in the surface energy is not obvious for basal planes and type II prism planes. This phenomenon can be explained by the fact that type I surfaces have a larger number of dangling bonds which become saturated after the adsorption of the metal atom. It can also be observed that type II facets have higher surface energies than type I after Co or Ni adsorption. This is in sharp contrast to pure WC, which has higher surface energies for type I facets. Therefore, type I planes will change from short prismatic facets in the pure WC case to long prismatic facets in the Co and Ni absorbed cases, whereas type II planes will accordingly form the short prismatic facets of WC particles when the adsorption of Co and Ni is present. Furthermore, in general, the W-termination is favored for both prismatic and basal planes except the basal and type II prismatic facets under the carbon-rich condition with Co adsorption.

The equilibrium crystal shape is determined through the minimization of the total surface free energy at a given volume according to the Wulff construction rule [27]. The total surface energy of WC grain can be expressed as [30]:

$$3a_{long}t\sigma_{long} + 3a_{short}t\sigma_{short} + \frac{\sqrt{3}}{2}a_{long}^2(r^2 + 4r + 1)\sigma_{basal} \quad (7)$$

By minimization, we can get the shape factors

$$R = \frac{2\frac{\sigma_{long}}{\sigma_{short}} - 1}{2 - \frac{\sigma_{long}}{\sigma_{short}}} \quad (8)$$

$$K = \frac{2\sigma_{basal}(2r + 1)}{3\sigma_{long}(r + 1)} \quad (9)$$

where  $a_{long}$  and  $a_{short}$  are the lengths of the long and short prismatic facets viewed along the  $\langle 0001 \rangle$  direction, respectively, and  $\sigma_{long}$  and  $\sigma_{short}$  are their respective surface energies. Fig. 5 shows the shape factors  $r$  and  $k$  in both car-

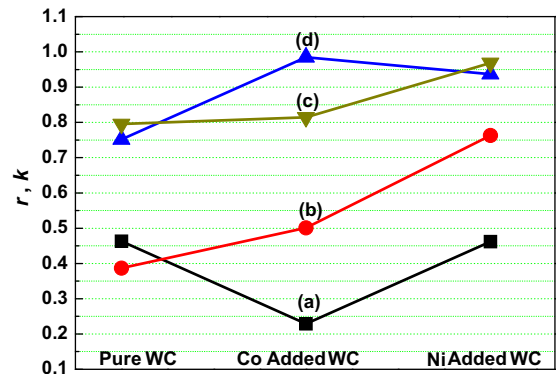


Fig. 5. (a) The  $r$  factor in the carbon-deficient condition, (b) the  $r$  factor in the carbon-rich condition, (c) the  $k$  factor in the carbon-deficient condition and (d) the  $k$  factor in the carbon-rich condition for pure WC, Co-added WC and Ni-added WC articles.

Table 2  
Calculated surface energies for basal and prism planes after Co and Ni adsorption on the surface at the most stable location\*.

Surface ID	Surface energy (eV Å <sup>-2</sup> )							
	Co adsorption				Ni adsorption			
	W <sub>2</sub> C (C deficient)		Graphite (C rich)		W <sub>2</sub> C (C deficient)		Graphite (C rich)	
	$E$	Location	$E$	Location	$E$	Location	$E$	Location
0001-W	<u>0.1979</u>	HC	0.2354	HC	<u>0.1515</u>	HC	<u>0.1890</u>	HC
0001-C	0.2238	H	<u>0.1863</u>	H	0.2518	H	0.2143	H
10 $\bar{1}$ 0-I-W	<u>0.1589</u>	BW	<u>0.2034</u>	BW	<u>0.1419</u>	BW	<u>0.1863</u>	BW
10 $\bar{1}$ 0-I-C	0.2918	BC	0.2473	BC	0.2975	BC	0.2531	BC
10 $\bar{1}$ 0-II-W	<u>0.2430</u>	H	0.2652	H	<u>0.1816</u>	H	<u>0.2038</u>	H
10 $\bar{1}$ 0-II-C	0.2763	BC	<u>0.2541</u>	BC	0.2346	BC	0.2124	BC

\* The locations of the possible sites for M are shown in Fig. 4. Only the most stable adsorption location is shown. For example, location HC for the 0001-W surface means that the Co or Ni atom will reside at the HC location because HC has the lowest energy after adsorption. The underlined numbers are the lowest energy for each type of the surface.

bon-rich and carbon-deficient conditions for pure WC, Co-adsorbed WC and Ni-adsorbed WC particles. Several interesting points are found from this figure. (i) As expected, the shape factors vary with the surface conditions (i.e. clean WC surface, Co-adsorbed WC surface and Ni-adsorbed surface). (ii) Under the same surface condition, the chemical potential of carbon affects the equilibrium shape of WC particles. (iii) The formation of truncated triangular prisms can be promoted with Co adsorption under the carbon-deficient condition because this condition gives the lowest  $r$  value. (iv) The formation of near-hexagonal prisms can be enhanced through Ni adsorption under the carbon-rich condition because this condition offers the largest  $r$  value. (v) The equilibrium shapes of WC crystals under all conditions (especially with Co or Ni adsorption) can be described as “bulky” because their  $k$  factors are near 0.8 or higher and thus the thickness of the truncated triangular prism and the width of its basal plane are similar, which is far from the platelet geometry.

#### 4.3. Comparisons between the simulation and experiment

Fig. 6a and b shows the XRD patterns of the as-received WC–Co powder and H<sub>2</sub>-treated powder, respectively. We note that the as-received powder consists of only WC and Co. The 0.2% C in the as-received powder cannot be detected because of its low concentration or being in an amorphous state. After heating in H<sub>2</sub>, however, W<sub>2</sub>C and Co<sub>6</sub>W<sub>6</sub>C phases are found in the XRD pattern. Chemical analysis of the powders shows that the total carbon concentration decreases from 5.75 to 5.18% after heating in H<sub>2</sub>. Based on the XRD and elemental analyses, one can safely say that the H<sub>2</sub>-treated powder is indeed in the carbon-deficient condition.

As mentioned in the experimental section, the growth of both carbon-rich and carbon-deficient WC–Co powders is conducted at 1400 °C under an argon atmosphere in a loose powder form (to minimize sintering). Furthermore, a graphite crucible is used in the carbon-rich condition

because the graphite crucible can supply carbon or prevent carbon loss from WC–Co powders during heating, thereby maintaining the carbon-rich condition in the entire heating process. It is well known that a ternary liquid phase forms at ~1320 °C for WC–Co cermets [45,46] and liquid Co wets WC well with a near-zero dihedral angle [47,48]. Therefore, it is expected that during heating at 1400 °C a thin liquid Co layer may wet some of WC particles. Alternatively, Co atoms will adsorb on WC surfaces via vapor transport since the vapor pressure of metals increases significantly at the onset of melting [49]. These expectations are consistent with the energy-dispersive spectroscopy (EDS) analysis. As shown in Fig. 7, Co is present everywhere for both carbon-rich and carbon-deficient WC–Co powders after heating in Ar at 1400 °C for 2 h. Therefore, the 1400 °C-treated samples can be considered as Co-adsorbed WC particles under either the carbon-rich or the carbon-deficient condition.

Fig. 8a and b shows the SEM images for WC–Co powders in both carbon-rich and carbon-deficient conditions before the treatment at 1400 °C. The powders are in the 100–700 nm range without noticeable facets for both conditions. Shown in Fig. 8c and d are the SEM images for carbon-rich and carbon-deficient WC–Co powders after 1400 °C growth, respectively. We note that some powder particles have grown to 1.0–2.0 μm in size, while many remain in the range of 0.5 μm or lower. The spread in the particle size is not unexpected because the growth of larger particles takes place at the expense of smaller particles. Since the crystal growth is not yet completed, the shape of large particles may or may not be the equilibrium morphology of WC particles, depending on whether the crystal growth is controlled kinetically or thermodynamically. Nevertheless, it is still beneficial to compare the shape of the large particles in the experiments with the simulation results because large particles have gone through sufficient growth and relaxation processes and therefore have the potential to be close to the equilibrium structures. Thus, the experimental  $r$  and  $k$  factors are estimated based on the measurements of the large particles obtained from multiple SEM images. Fig. 8c and d shows the representative images of these large particles. Note that the truncated triangular prism appears in both types of powders. However, the  $r$  factors for the two powders are different. For the carbon-rich powder, the short prismatic facets are ~0.4 times the length of the long prismatic facets, which is close to the theoretical prediction shown in Fig. 5. For the carbon-deficient powder, the  $r$  factor from the SEM image is in the range of 0.2–0.3, which is also in good agreement with the theoretical value of 0.23 (Fig. 5). These results reveal that the chemical potential of carbon can affect the morphology of WC particles. Moreover, the length ratio of the short prismatic facet to the long prismatic facet is close to the equilibrium values during the growth of WC particles under both carbon-rich and carbon-deficient conditions with the absorption of Co. However, the ratios of the thickness of the truncated WC prism to the width of the basal plane, i.e. the  $k$  factor, in both powders are small-

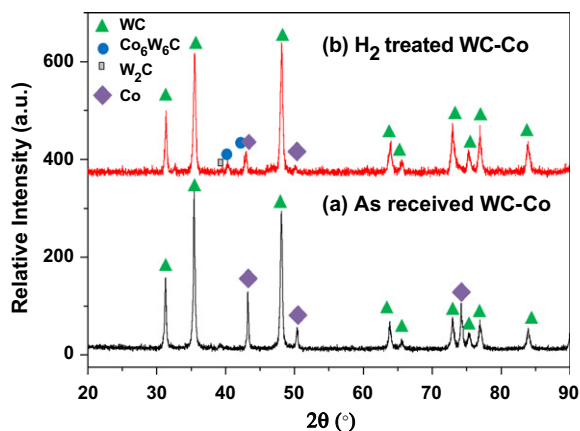


Fig. 6. XRD patterns for (a) the as-received WC–Co powder and (b) the as-received WC–Co powder after heating in an H<sub>2</sub> atmosphere for 2 h at 800 °C.

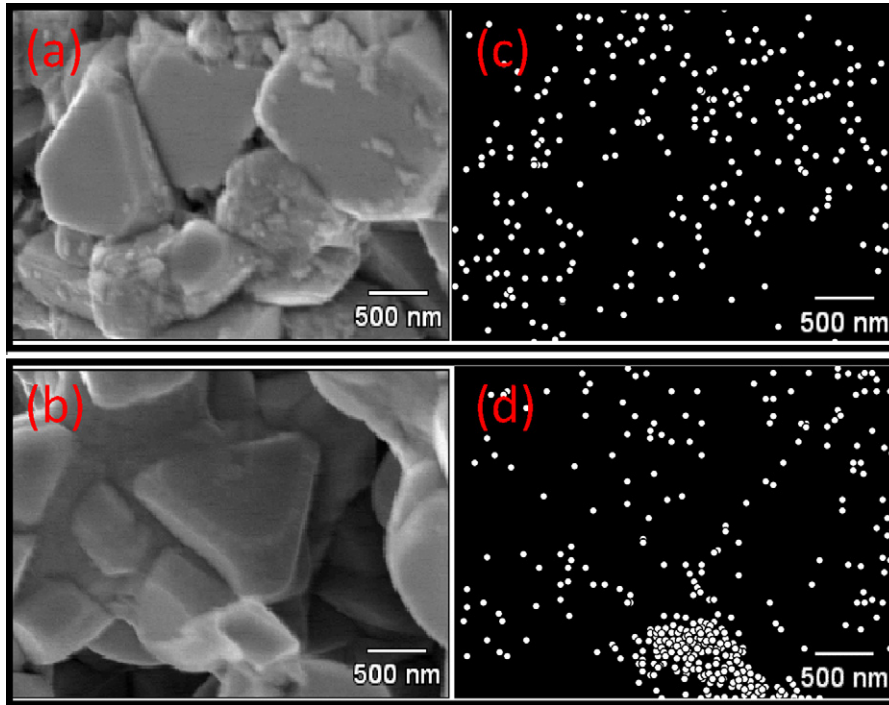


Fig. 7. (a) and (b) SEM images with (c) and (d) the corresponding EDS mapping of the Co element for WC-Co powders after heating at 1400 °C in an Ar atmosphere under (a) and (c) the carbon rich condition and (b) and (d) the carbon deficient condition. The white dots in (c) and (d) represent the presence of the Co element.

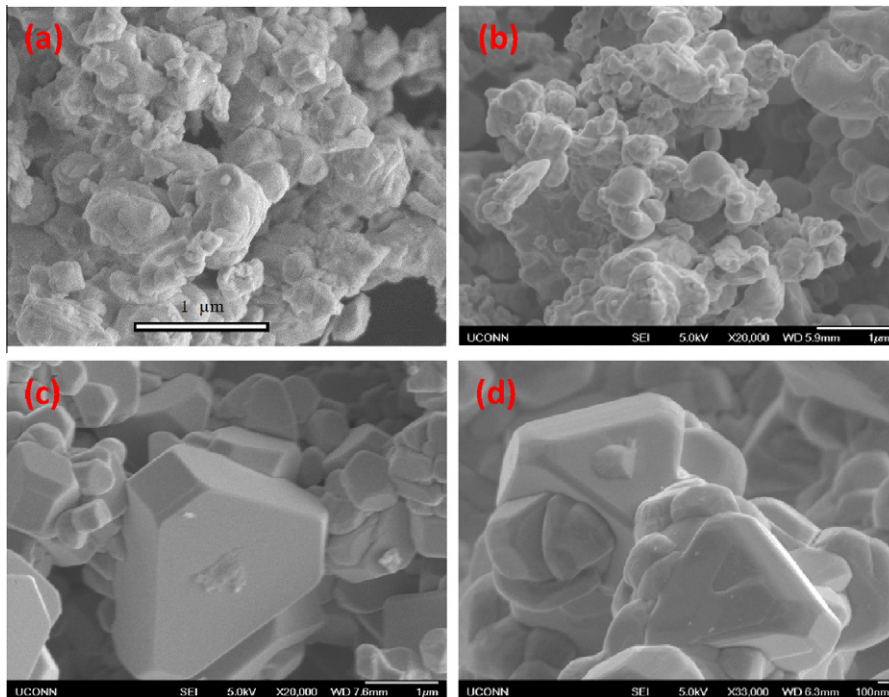


Fig. 8. SEM images of the commercial WC-Co powder: (a) the as-received, (b) after H<sub>2</sub> treatment at 800 °C, (c) after heating in Ar at 1400 °C for 2 h of the as-received powder and (d) after H<sub>2</sub> treatment at 800 °C and then heating in Ar at 1400 °C for 2 h.

ler than those predicted from the first-principles calculation (Fig. 5). One possible mechanism for the discrepancy in the  $k$  factor between the experiment and simulation is the slow growth kinetics along the  $[0\ 0\ 0\ 1]$  direction.

Before closing, it should be pointed out that the trend of the  $r$  factor predicted in the present study is the opposite of that predicted previously by Christensen et al. [29,30]. In other words, the present DFT calculations (Fig. 5) predict

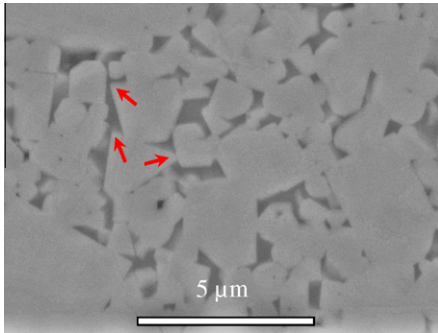


Fig. 9. SEM image of the WC–Co body sintered at 1450 °C for 24 h in argon using the as-received commercial powder under the carbon-rich condition. The arrows indicate the presence of the pointed edges, i.e. a small  $r$  factor, in the partially developed triangular prisms. The triangular prisms are not fully developed, presumably due to the presence of the neighboring WC particles, which block the growth of some WC edges.

that, in the presence of Co adsorption, the carbon-deficient condition leads to a smaller  $r$  factor than the carbon-rich condition, while the DFT calculations by Christensen et al. [29,30] predict an opposite trend. We believe that the different trends stem from the different simulation conditions. The DFT calculations by Christensen et al. [29,30] applies to liquid-phase sintering, i.e. WC particles are surrounded by liquid Co. In contrast, the present simulation deals with the adsorption of Co atoms on WC particles. These different simulation conditions result in different trends for the  $r$  factor. To ensure that such different trends are supported by experiments, the as-received WC–5.8 wt.% Co powder under the carbon-rich condition was sintered at 1450 °C in argon for 24 h. As shown in Fig. 9, partially developed triangular prisms (viewed from the  $(0\ 0\ 0\ 1)$  basal plane) are present in the sintered body. This is in sharp contrast to the truncated triangular prisms of WC particles shown in Fig. 8c when WC particles grow in a loose powder form. These experimental results indicate that the morphology of WC particles at the carbon-rich condition indeed depends on how Co interacts with the WC surface, i.e. liquid phase vs. atomic adsorption, providing support to the correctness of both DFT simulations.

## 5. Concluding remarks

The equilibrium shape of WC particles is studied using the *ab initio* DFT calculation. The effects of the carbon chemical potential and the adsorption of Co and Ni atoms on the surface of WC particles are investigated. The major conclusion from this study is that the equilibrium shape of WC particles under the condition of little or no liquid phase is “bulky”, suggesting that the platelet morphology of WC crystals formed in the solid state is not the equilibrium structure. Furthermore, the binder metal selection and the chemical potential of carbon affect the equilibrium morphology of WC crystals strongly. The more detailed conclusions derived from this study are as follows.

1. The equilibrium shape of WC particles is a truncated triangular prism, with its surfaces consisting of the  $(0\ 0\ 0\ 1)$  basal planes, type I  $(1\ 0\ \bar{1}\ 0)$  and type II  $(1\ 0\ \bar{1}\ 0)$  planes under both carbon-rich and carbon-deficient conditions.
2. The adsorption of Co and Ni on the WC surface alters the dimensions of the WC surface facets. Co adsorption under the carbon-deficient condition promotes the formation of truncated triangular prisms, whereas Ni adsorption under the carbon-rich condition enhances the formation of near-hexagonal prisms.
3. The chemical potential of carbon also has a large influence on the dimensions of the WC surface facets. In the presence of Co adsorption, the carbon-deficient condition results in more pointed truncated triangular prisms than the carbon-rich counterpart because the  $r$  factor for the carbon-deficient condition is much smaller than that for the carbon-rich condition.
4. The  $k$  factors for Co- and Ni-adsorbed WC particles are 0.8 or higher regardless of the carbon condition. Thus, the equilibrium shapes of WC crystals with Co or Ni adsorption can be described as “bulky” rather than “plate-like” because the thickness of the truncated triangular prism and the width of its basal plane are similar.
5. The experiments with the coarse-grained WC–Co powder reveal that the  $r$  factor of WC particles is close to the equilibrium value during the growth of WC particles under both carbon-rich and carbon-deficient conditions. However, the  $k$  factor is much smaller than those predicted from the first-principles calculation, suggesting slow growth kinetics along the  $[0\ 0\ 0\ 1]$  direction of the WC crystal.

## Acknowledgements

This research was sponsored by the US National Science Foundation (NSF) under the contract number CMMI-0856122. The support and vision of Dr. Mary Toney is greatly appreciated.

## References

- [1] Schwarzkopf P, Kieffer R. Refractory hard metals. New York: The Macmillan Company; 1953. p. 138–161.
- [2] Jack DH. In: Schwartz MM, editor. Engineering applications of ceramic materials: source book. Materials Park, OH: American Society for Metals; 1985. p. 147–53.
- [3] Metals Handbook, vol. 3. Properties and selection: stainless steels, tool materials and special-purpose metals. 9th ed. Materials Park, OH: American Society for Metals; 1980.
- [4] Yih SWH, Wang CT. Tungsten sources, metallurgy, properties and applications. New York: Plenum Press; 1979.
- [5] Fang ZZ, Wang X, Ryu R, Hwang KS, Sohn HY. Int J Refract Met Hard Mater 2009;27:288.
- [6] Porat R, Berger S, Rosen AS. Mater Sci Forum 1996;225-227 (Pt 1):629.
- [7] Bartha L, Atato P, Toth AL, Porat R, Berger S, Rosen A. J Adv Mater 2000;32(3):23.
- [8] Fang ZZ, Eason JW. Int J Refract Metal Hard Mater 1995;13(5):297.

- [9] Azcona I, Ordonez A, Sanchez JM, Castro F. *J Mater Sci* 2002;37(19):4189.
- [10] Densley JM, Hirth JP. *Scripta Mater* 1997;38(2):239.
- [11] Jia K, Fischer TE, Gallois B. *Nanostruct Mater* 1998;10(5):875.
- [12] Weidow J, Norgren S, Andren HO. *Int J Refract Met Hard Mater* 2009;27:817.
- [13] Exner HE. *Int Met Rev* 1979;24:149.
- [14] Bonache V, Salvador MD, Busquets D, Burguete P, Martinez E, Sapina F, et al. *Int J Refract Met Hard Mater* 2011;29:78.
- [15] Sun L, Jia CC, Xian M. *Int J Refract Met Hard Mater* 2007;25:121.
- [16] Yoon BW, Lee BA, Kang SJL. *Acta Mater* 2005;53:4677.
- [17] Olson JM, Makhlof MM. *J Mat Sci* 2001;36:3027.
- [18] Sommer M, Schubert W, Zobetz E, Warbichler P. *Int J Refract Met Hard Mater* 2002;20:41.
- [19] Wang X, Fang ZZ, Sohn HY. *Int J Refract Met Hard Mater* 2008;26:232.
- [20] Gothelid M, Haglund S, Argen J. *Acta Mater* 2000;48:4358.
- [21] Wang Y, Heusch M, Lay S, Allibert CH. *Phys Stat Sol (a)* 2002;193:271.
- [22] Weidow J, Andren HO. *Acta Mater* 2010;58:3888.
- [23] Delano A, Bacia M, Pauty E, Lay S, Allibert CH. *J Crystal Growth* 2004;270:219.
- [24] Kim CS, Rohrer GS. *Interface Sci* 2004;12:19.
- [25] Shatov AV, Firstov SA, Shatova IV. *Mater Sci Eng A* 1998;242:7.
- [26] Shatov AV, Ponomarev SS, Firstov SA, Warren R. *Int J Refract Met Hard Mater* 2006;24:61.
- [27] Wulff G. *Z Kristallogr Mineral* 1901;34:449.
- [28] Christensen M, Wahnstrom G. *Phys Rev B* 2003;67:115415.
- [29] Christensen M, Wahnstrom G, Allibert C, Lay S. *Phys Rev L* 2005;94:066105.
- [30] Christensen M, Wahnstrom G, Lay S, Allibert C. *Acta Mater* 2007;55:1515.
- [31] Arato P, Bartha L, Porat R, Berger S, Rosen A. *Nanostruct Mater* 1998;10:245.
- [32] Laptev AV. *Powder Metall Met Ceram* 2007;46:415.
- [33] Nelson RJ, Milner DR. *Powder Metall* 1971;14:39.
- [34] Menéndez E, Sort J, Concustell A, Surinach S, Nogués J, Baró MD. *Nanotechnology* 2007;18:185609.
- [35] Da Silva AGP, Schubert WD, Lux B. *Mater Res* 2001;4:59.
- [36] Meredith B, Milner DR. *Powder Metall* 1976;1:38.
- [37] Ban ZG, Shaw LL. *Acta Mater* 2001;49:2933.
- [38] Kresse G, Hafner J. *Phys Rev B* 1993;47:558.
- [39] Kresse G, Furthmuller J. *Phys Rev B* 1996;54:11169.
- [40] Perdew JP, Chevary JA, Vosko SH, Jackson KA, Pederson MR, Singh DJ, et al. *Phys Rev B* 1992;46:6671.
- [41] Price DL, Cooper BR. *Phys Rev B* 1989;39:4945.
- [42] Zhu H, Aindow M, Ramprasad R. *Phys Rev B* 2009;80:201406 (R).
- [43] Suetin DV, Shein IR, Kurlov AS, Gusev AI, Ivanovski AL. *Phys Solid State* 2008;50:1420.
- [44] Ban ZG, Shaw LL. *J Mater Sci* 2002;37:3397.
- [45] Froschauer L, Fulrath RM. *J Mater Sci* 1976;11:142.
- [46] Snowball RF, Milner DR. *Powder Metall* 1968;11:23.
- [47] Humenik Jr M, Parikh NM. *J Am Ceram Soc* 1956;39:60.
- [48] Parikh NM, Humenik Jr M. *J Am Ceram Soc* 1957;40:315.
- [49] Gaskell DR. *Introduction to thermodynamics of materials*. 3rd ed. London: Taylor & Francis; 1995.